Revealing charge anisotropies in metal compounds via high-purity x-ray polarimetry

Lena Scherthan,[1] Juliusz A. Wolny,[1] Isabelle Faus,[1] Olaf Leupold,[2] Kai S. Schulze,[3,4,5] Sebastian Höfer,[3,4] Robert Loetzsch,[3,4] Berit Marx-Glowna,[3,4,5] Christopher E. Anson,[6] Annie K. Powell,[6,7] Ingo Uschmann,[3,4,5] Hans-Christian Wille,[2] Gerhard G. Paulus,[3,4,5] Volker Schünemann,[1] and Ralf Röhlsberger[3,5,4,2]

[1]*Fachbereich Physik, RPTU University of Kaiserslautern-Landau, Erwin-Schrödinger Straße 46, 67663 Kaiserslautern, Germany*

[2]*Deutsches Elektronen-Synchrotron DESY, Notkestraße 85, 22607 Hamburg, Germany*

[3]*Helmholtz-Institut Jena, Fröbelstieg 3, 07743 Jena, Germany*

[4]*Institut für Optik und Quantenelektronik, Friedrich-Schiller-Universität Jena, Max-Wien-Platz 1, 07743 Jena, Germany*

[5]*Helmholtz Centre for Heavy Ion Research (GSI), Planckstraße 1, 64291 Darmstadt, Germany*

[6]*Institut für Anorganische Chemie, Karlsruher Institut für Technologie (KIT), Engesserstrasse 15, 76131 Karlsruhe, Germany*

[7]*Institut für Nanotechnologie, Karlsruher Institut für Technologie (KIT), Hermann-von-Helmholtz-Platz 1, 76344 Eggenstein-Leopoldshafen, Germany*

(Received 25 September 2017; accepted 4 May 2026; published 15 June 2026)

Linear polarization analysis of hard x-rays is employed to probe electronic anisotropies in metal-containing complexes with high selectivity. We use polarization-resolved nuclear forward scattering (PR-NFS) of synchrotron radiation at the 14.4 keV nuclear resonance of ^{57}Fe to determine electric field gradients (EFGs) in an iron(II) spin-crossover compound as they evolve during a temperature-dependent high-spin/low-spin transition. A pair of crossed Si(840) channel-cut crystals provides a high-purity x-ray polarimeter that suppresses the nonresonant background by nearly nine orders of magnitude and enables selective detection of nuclear resonant $\sigma \rightarrow \pi$ scattering. Using the spin-crossover complex $Fe(PM\text{-}BiA)_2(NCS)_2$ as a model system, we determine the orientation of the EFG tensor in the high-spin and low-spin states and follow its reorientation across the gradual thermally driven spin transition. By choosing suitable sample orientations, the polarization selectivity enhances the signal of a high-spin minority fraction of a few percent at low temperature. It reveals that the high-spin EFG at 120 K is not randomly distributed and does not align with the dominant low-spin EFG when these high-spin centers form a minority phase embedded in a low-spin matrix. The combination of PR-NFS with dynamical NFS simulations and density-functional calculations thus provides a sensitive, element- and site-selective method to quantify electronic anisotropies and their changes across phase transitions in Mössbauer-active metal compounds.

DOI: 10.1103/rj8d-86dj

I. INTRODUCTION

The knowledge of charge distributions and their anisotropies in molecules is crucial for understanding and precise modeling of molecular interactions and optical properties of chemical systems [1]. Powerful spectroscopic methods to investigate charge anisotropies in molecules are optical linear dichroism and birefringence that rely on probing the orientation dependence of the interaction of linearly polarized light with matter [2]. For example, optical linear dichroism is applied to follow the orientation or reorientation of molecular systems resulting from external stimuli, like any reaction that involves changing the structure or length of a molecule or structural phase transitions in molecular solids [3,4]. For a microscopic analysis of charge distributions in molecules, however, one needs to apply optical techniques capable of probing atomic length scales.

The availability of highly brilliant synchrotron radiation sources has facilitated the transfer of linear and circular dichroism to the regime of hard x-rays [5,6]. Today, x-ray linear and circular dichroism are very powerful techniques to probe charge and spin order in condensed matter with elemental specificity and site selectivity [7,8]. Dichroic spectroscopies probe the imaginary part of the anisotropic index of refraction n by comparing the incoherent absorption of two orthogonal polarization states. The same information is also contained in the real part of n that leads to a rotation of the plane of polarization when two orthogonal polarization components experience different coherent phase shifts, an effect well known as optical birefringence. The analysis of birefringence in the x-ray regime, however, is much less common than x-ray dichroism, because efficient polarization analysis at energies of hard x-rays requires some significant technical effort. On the other hand, it opens a series of advantages compared to dichroism, because (1) it can be combined with momentum-resolving methods for high spatial resolution, (2) it does not require two subsequent measurements with different polariza-

Published by the American Physical Society under the terms of the Creative Commons Attribution 4.0 International license. Further distribution of this work must maintain attribution to the author(s) and the published article's title, journal citation, and DOI.

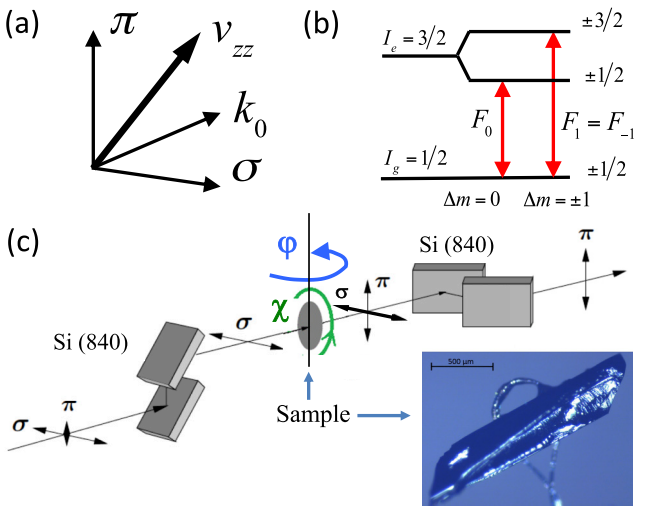


FIG. 1. (a) Sketch of the NFS geometry, where $\boldsymbol{k}_0$, $\boldsymbol{\sigma}$, $\boldsymbol{\pi}$, and $\boldsymbol{v}_{zz}$ are unit vectors of the photon wave vector, the linear polarization basis, and the main component of the electric field gradient in the sample, respectively. (b) Nuclear level scheme of ^{57}Fe for the case of a pure electric hyperfine interaction. (c) Experimental setup for PR-NFS experiments, consisting of two polarizing Si(840) channel-cut crystals that are aligned in a 90° crossed setting to detect $\sigma \rightarrow \pi$ scattering from the sample located in between. In the experiment, the transmission through the polarimeter is monitored as a function of the sample orientation, adjusted via the angles φ and χ. The image at the bottom right shows a micrograph of the sample crystal.

tion states that allows for time-resolved measurements, e.g., in pump-probe schemes, and (3) it promises to obtain significantly higher signal-to-noise ratios.

Polarimetry in the vicinity of nuclear resonances has been shown to be a very sensitive technique to detect tiny changes in the polarization state of x-rays caused by the interaction with an anisotropic or chiral, thus optically active medium [9–11]. This applies, in particular, for the high-purity variant of it [12,13]. The technique relies on the application of x-ray linear Bragg polarizers in a 90° crossed setting with purities in the range of 10^{-10} [14]. This method has the highest sensitivity when applied at atomic absorption edges [15–17] or nuclear resonances [18–23]. It can be combined with a set of focusing and recollimating compound refractive lenses between the linear polarizers to generate micrometer-sized focal spots at the sample position without compromising the polarization purity of the polarimeter [24].

Here, we employ polarization-resolved nuclear forward scattering (PR-NFS) of synchrotron radiation at the 14.4-keV nuclear resonance of ^{57}Fe to probe atomic charge anisotropies in a metal compound. If the charge anisotropy in the system leads to an electric field gradient (EFG) at the ^{57}Fe nucleus, nuclear states with a finite electrical quadrupole moment are subject to an electric hyperfine interaction. As a result, the excited nuclear state of ^{57}Fe splits into two sublevels, shown in Fig. 1(b), which leads to a pronounced optical activity in the vicinity of the nuclear resonance. The nuclear resonant forward scattering amplitude $\mathbf{f}_r$ is given by [25]

$$\mathbf{f}_r \sim F_1\,\mathbf{I} + \begin{pmatrix} (\boldsymbol{\pi}\cdot\boldsymbol{v}_{zz})^2 & (\boldsymbol{\sigma}\cdot\boldsymbol{v}_{zz})(\boldsymbol{\pi}\cdot\boldsymbol{v}_{zz}) \\ (\boldsymbol{\sigma}\cdot\boldsymbol{v}_{zz})(\boldsymbol{\pi}\cdot\boldsymbol{v}_{zz}) & (\boldsymbol{\sigma}\cdot\boldsymbol{v}_{zz})^2 \end{pmatrix}[F_0 - F_1], \tag{1}$$

where $\mathbf{I}$ is the (2×2) unity matrix, $\boldsymbol{v}_{zz}$ is a unit vector along the main axis of the electric field gradient, $\boldsymbol{\sigma}$ and $\boldsymbol{\pi}$ are the linear polarization basis vectors [see Fig. 1(a)], and F_0, F_1 describe Lorentzian functions that represent the resonant transitions between the nuclear ground state and the two levels of the excited nuclear state with $\Delta m = 0$ and $\Delta m = \pm 1$, respectively. If the main axis of the EFG is not parallel or perpendicular to the incident linear σ polarization, the off-diagonal elements of the matrix quantity $\mathbf{f}_r$ are nonzero and the polarization state of the transmitted radiation turns out to be elliptical. Thus, probing the π component of the transmitted radiation in a setup with two crossed polarizers provides a sensitive measure of the orientation of the EFG relative to the plane of linear polarization of the incident light. This property is exploited here to probe the reorientation of electrical field gradients upon a high-spin (HS, $S = 2$) to low-spin (LS, $S = 0$) transition in an iron(II)-containing spin-crossover (SCO) compound [26].

The spin state of iron(II) SCO compounds can be switched reversibly from the LS state to the HS state by variation of temperature and pressure, or by irradiation with light [27–29]. More recently, the spin-dependent charge-transport properties of SCO molecules have also generated interest for their use in spintronic devices [30,31]. Indeed, a giant resistance change across the phase transition in SCO materials of more than 3000% has been calculated theoretically [32]. Although not yet realized, it can be envisioned that the spin-dependent charge and/or spin-transfer properties of such devices may be tuned by variable concentrations of minority HS defect sites in a matrix of LS centers or vice versa. Therefore, it is of pivotal interest to have a spectral method at hand that is able to probe specifically spin-dependent changes in the electronic anisotropy of minority spin species in SCO compounds.

II. METHODS

As a model for PR-NFS at the 14.4 keV nuclear resonance of ^{57}Fe, the SCO compound $[Fe(PM\text{-}BiA)_2(NCS)_2]$ [33] was chosen as a reference. This compound shows a thermally inducible, reversible spin-state transition between the LS and the HS state in the range 150–230 K for powder samples. In the HS state, it exhibits a pure electric hyperfine interaction caused by a large electric field gradient (EFG) at the position of the Fe atom typical for high-spin octahedral Fe(II) complexes [26,33]. A single crystal of $[Fe(PM\text{-}BiA)_2(NCS)_2]$, enriched to 95% in ^{57}Fe, was grown from dichloromethane/ethanol/diethyl ether. The monoclinic phase of the synthesized single crystals, with four molecules in its unit cell (see Appendix A) was confirmed by X-ray crystallographic measurements. This phase shows a gradual SCO behavior [33,34] with an almost pure HS state at 220 K and above, which is confirmed by conventional transmission Mössbauer data (see Appendix G) taken from a powder sample that was taken for the growth of the single crystal used here.

The experiments were carried out at beamline P01, PETRA III, DESY, Hamburg [35] in 60-bunch mode of operation, providing a bunch separation of 128 ns. The energy of the synchrotron radiation was tuned to the 14.4-keV resonance of ^{57}Fe with a bandwidth of about 1 eV using a Si(111) double-crystal monochromator. The experimental setup is schematically shown in Fig. 1(c). For the PR-NFS experiments, the sample and its environment are located between two polarizing, four-bounce Si(840) channel-cut crystals that were cut with an asymmetry angle of -28.1° to optimally transmit the incident x-ray beam. The two channel-cut crystals are aligned in crossed setting in order to detect nuclear resonant $\sigma \rightarrow \pi$ scattering. Due to the very high suppression of the nonresonant σ-polarized background to a level on the order of 10^{-9}, no high-resolution monochromator was needed to perform these experiments. The energetic bandpass of the (840) reflection at these crystals is 43 meV with 75% peak transmission, constituting a significant energetic bandpass reduction to avoid radiation damage at the sample.

Orientation-dependent NFS and PR-NFS experiments at various temperatures were performed with the sample mounted on a Eulerian Cradle for angular orientation [see Fig. 1(c)], whereby the cooling of the sample down to temperatures in the range of 100 K was performed by the use of an N_2 cryogenic gas stream [36]. A series of NFS time spectra of the SCO compound were taken at room temperature without polarization analyzer for selected orientations of the sample to confirm the magnitude of the quadrupole splitting $\Delta E_Q = 2.58$ (± 0.02) mm/s, asymmetry parameter $\eta = 0.3(\pm 0.2)$ in the Fe(II) HS state (see Fig. 6).

The asymmetry parameter η was determined from the CONUSS analysis of the orientation-dependent NFS time spectra, where it enters the full (2×2) forward scattering matrix through the relative weights of the $\Delta m = 0$ and $\Delta m = \pm 1$ transitions. For a single-crystal measurement at multiple orientations, η can be constrained because a nonzero value modifies the angular dependence of the $\sigma \rightarrow \pi$ scattering intensity beyond the simple $\sin^2\chi \cos^2\chi$ pattern predicted for an axially symmetric EFG ($\eta = 0$). Density functional calculations (DFT) [37] for the HS state yield a comparable value.

III. RESULTS AND DISCUSSION

High-purity polarimetry was then performed to determine the direction of the electric field gradients in the sample. A series of PR-NFS spectra taken at $T = 220$ K are shown in Fig. 2(a). For each orientation χ, the data exhibit a temporal beat pattern resulting from a quadrupole splitting of $\Delta E_Q = 2.64$ (± 0.15) mm/s. Values for ΔE_Q determined here from the temporal beat patterns recorded at various temperatures are consistent (within the error margin) with those determined from conventional transmission Mössbauer spectroscopy (see Appendix G).

In addition to the time-dependent NFS and PR-NFS spectra, the time-integrated PR-NFS signal was recorded as a function of the angle χ, while the angle φ was kept fixed (from now on referred to as χ-PR-NFS scans). In Fig. 2(b), such a χ-PR-NFS scan for $\varphi = 0^\circ$ is shown. In accordance with the PR-NFS spectra, this χ-PR-NFS scan exhibits a

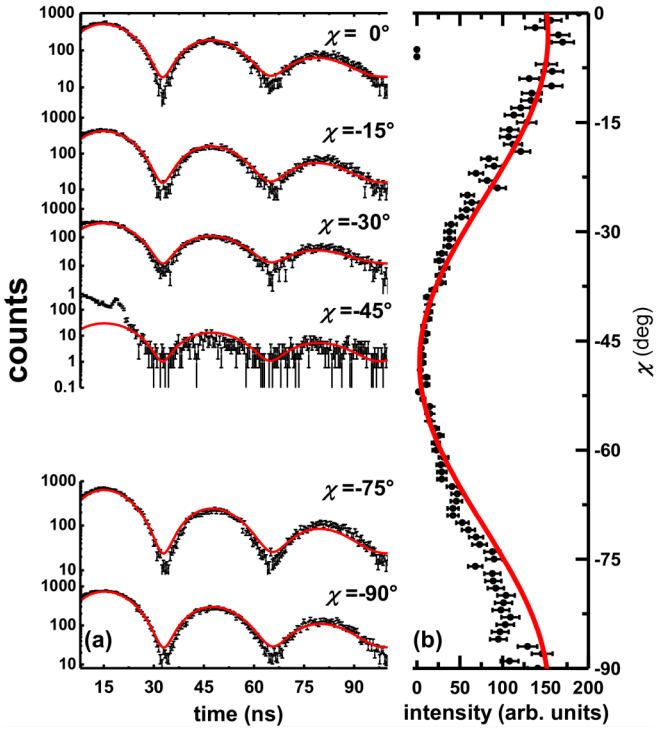


FIG. 2. (a) PR-NFS spectra recorded for selected orientations χ of the single crystal at $T = 220$ K and $\varphi = 0$ (black). The red lines show theoretical calculations of the scattered amplitude assuming a pure HS state with $\Delta E_Q = 2.64$ (± 0.15) mm/s and $\eta = 0.3$ (± 0.2). (b) Corresponding χ-PR-NFS scan with theoretical calculation (red line) showing clearly the orientation dependence of the nuclear resonant $\sigma \rightarrow \pi$ scattering. Parameters are given in Table III. The deviation between the simulation and the measured data for χ =–45° is due to a spurious bunch and electronic noise. The systematic deviations for $\chi < -65^\circ$ are attributed to small drifts in the polarization-analyzer alignment during the continuous χ scan and to the finite asymmetry parameter η, which introduces corrections to the idealized $\sin^2\chi \cos^2\chi$ angular dependence of Eq. (D1).

minimum at $\chi \sim -45^\circ$, which means that at this angle the main component of the EFG is either parallel or perpendicular to the incident linear σ polarization. When the sample is oriented at either $\chi \sim 0^\circ$ or $\chi \sim -90^\circ$, the off-diagonal elements of $\mathbf{f}_r$ are maximized. Consequently, the time-integrated χ-PR-NFS scan has a maximum and the time-dependent PR-NFS spectrum shows a quantum beat pattern characteristic of an HS species. Thus, the χ-PR-NFS scans clearly demonstrate the sensitivity of the $\sigma \rightarrow \pi$ scattering process to the atomic charge anisotropy at the position of the ^{57}Fe nucleus. Furthermore, these PR-NFS scans, delivering a full orientation dependence, are less time consuming (~30 min per scan over a φ range of 180° at RT) than taking NFS or PR-NFS time spectra for several orientations [~10 min per orientation (φ, χ) at a countrate of ~500 s^{-1} at RT]. Therefore, we recorded a series of χ-PR-NFS scans over a χ interval from 0° to −160° for different values of φ, as shown in Fig. 3(a). The positions of the maxima/minima in the χ-PR-NFS scans display a pronounced dependence on the sample orientation φ, as shown in Fig. 3(b). The corresponding minima positions χ_{Min} and fit parameters χ_0 are summarized in Table IV.

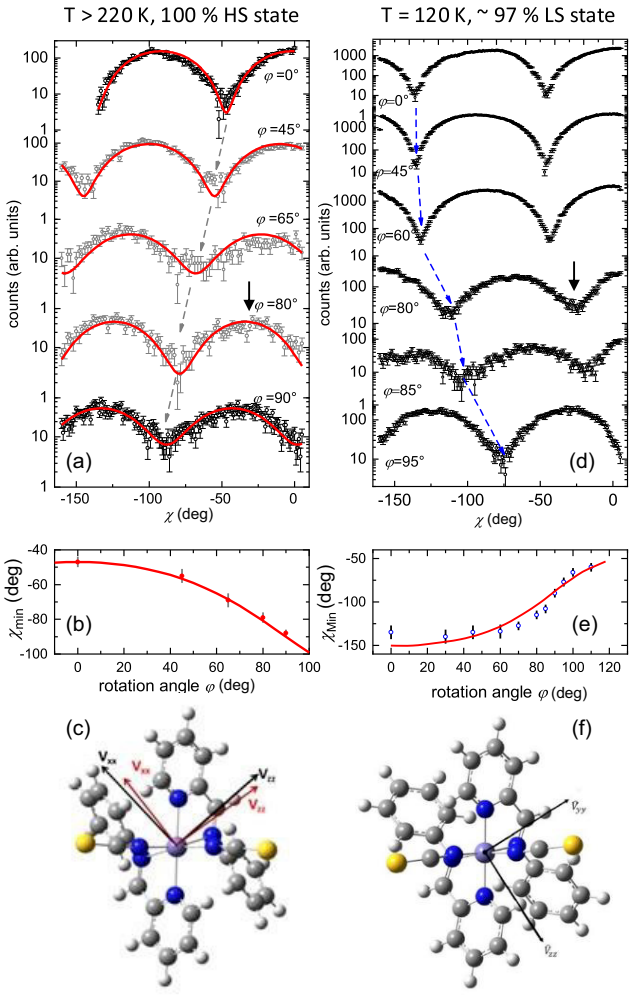


FIG. 3. (a), (d) Nuclear resonant σ-π scattering (χ-PR-NFS scans) taken at temperatures $T \geqslant 220$ K [panel (a)] and $T = 120$ K [panel (d)] for selected orientations φ. The temperature-dependent change of the χ-PR-NFS scans proves the reorientation of the EFG upon the SCO transition from the HS state (left panel) to the LS state (right panel). The dashed lines are guides to the eye to trace the shift of two minima of the curves for the HS and the LS states, respectively. The figures below panels (b) and (e) display the shift of these minima as a function of the rotation angle φ, starting at $\varphi = 0$. (c), (f) Schematic representation of $[Fe(PM\text{-}BiA)_2(NCS)_2]$ with the orientation of the EFG at the site of the Fe atom in the HS state [panel (c)] and the LS state [panel (f)] determined via a DFT calculation assuming C_2 symmetry (black vectors). The viewing direction, which corresponds to the direction of the V_{yy} component of the HS EFG and to the V_{xx} component of the LS EFG, is along the c axis of the single crystal. For the HS state, the red arrows show the EFG orientation as determined from the experimental data. The solid red lines in panel (a) are fits according to Eq. (D1), those in panels (b) and (e) are fits according to Eq. (D3), taking the EFG orientations shown in panels (c) and (f) as configuration at $\varphi = 0$. Parameters are given in Tables IV and V.

The detailed analysis of these data with the use of the dynamical theory of nuclear forward scattering [38,39] [solid red lines in Figs. 3(a) and 3(b) are simulations according to Eqs. (D1) and (D3), respectively] yields the EFG orientation

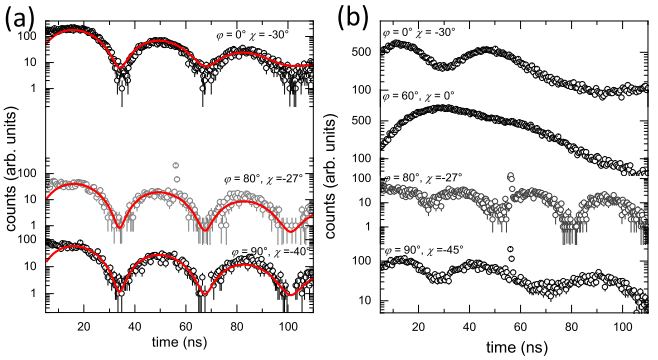


FIG. 4. PR-NFS beat patterns taken (a) at temperatures $T \geqslant 220$ K (gray: room temperature, black: $T = 220$ K) and (b) at $T = 120$ K, for selected orientations (φ, χ). While the data in panel (a) all show the quantum beat pattern characteristic of the quadrupole splitting ΔE_Q of the HS state, the beat pattern of the data taken at $T = 120$ K is strongly orientation dependent, indicating a superposition of contributions from the LS state in the majority phase and the HS state in a ≈3% minority phase with different EFG orientations [41].

of the HS state in the molecular coordinate system [Fig. 3(c)] and reproduces all obtained NFS time spectra taken at room temperature [see Fig. 6]. The EFG's main axis system of the molecular HS state determined in this way is depicted in Fig. 3(c) together with a main axis system calculated by density functional calculations assuming a C_2 symmetry [40]. Allowing a tolerance of 5°, the theoretical calculation reproduces the experimentally determined EFG quite well. At $T = 120$ K, the monoclinic phase of $[Fe(PM\text{-}BiA)_2(NCS)_2]$ should be mostly in the LS state. In fact, orientation-dependent NFS data obtained at $T = 120$ K show that the majority of the iron centers are in their LS state that can be inferred from the low value of the quadrupole splitting $\Delta E_Q = 0.63$ (±0.02) mm/s (see Fig. 7).

Figure 3(d) displays χ-PR-NFS scans obtained at $T = 120$ K in a χ interval from 0° to −160°. Compared to the data in Fig. 3(a), the minima of the curves shift in opposite direction with increasing angle φ as displayed in Fig. 3(e). The corresponding minima positions are listed in Table V. This reflects a significant change of the EFG orientation as compared to the HS state that occurs during the SCO transition. Fig. 3(f) shows the result of a DFT calculation of the EFG for the LS state. The red line in Fig. 3(e) is a theoretical simulation according to Eq. (D3), considering the EFG of the DFT results as starting parameter for the analysis. While this curve qualitatively describes the measured data, deviations are clearly visible. An inspection of the PR-NFS time spectra at selected angular configurations (φ, χ) for the two temperature regimes, shown in Fig. 4, points to the origin of these deviations: For samples with large effective thickness, multiple coherent scattering leads to dynamical beats that modulate the time spectra in addition to the quantum beats arising from hyperfine splitting. In the present high-temperature measurements, the moderate effective thickness ($t_{\text{eff}} \approx 10$–$17$) keeps dynamical beats negligible, so that the time spectra are governed by quantum beats from the quadrupole interaction. At 120 K, the increased Lamb-Mössbauer factor raises t_{eff} to values of order 50–90 and dynamical

beats become significant, complicating the spectral analysis (see Appendix C).

To assess how well the low-temperature data can be reproduced from known input parameters, dynamical NFS simulations were performed using (1) the DFT-calculated LS EFG orientation as a starting point, (2) $\Delta E_Q(\mathrm{LS}) = 0.63$ mm/s from conventional Mössbauer spectroscopy, (3) the HS EFG parameters (ΔE_Q, Euler angles) determined from the high-temperature data, and (4) a HS minority fraction in the range of 3–7%. As shown in Appendix C (Fig. 7 and Table II), such constrained simulations can reproduce the NFS time spectra at 120 K for a subset of crystal orientations ($\varphi = 0°$, $\chi = 0°$ to $-60°$), yielding Mössbauer parameters consistent with the powder data. The simulation of the χ-PR-NFS scans in Fig. 3(d) using the DFT-derived LS EFG qualitatively captures the shift of the minima [red line in Fig. 3(e)], but quantitative deviations remain.

Model calculations (see Figs. 8 and 9) reveal that both the LS asymmetry parameter η and the precise HS minority fraction critically influence the contrast and the positions of the extrema in the χ-PR-NFS scans, which explains why the measured data at 120 K can be described equally well by multiple parameter sets. Consequently, a unique and internally consistent determination of the LS EFG orientation from the present dataset is not possible. This limitation, together with the complicating effect of dynamical beats from the large effective thickness at 120 K, motivates the experimental improvements outlined below.

In contrast to the high-temperature data in Fig. 4(a), the time spectra in Fig. 4(b) taken at 120 K are strongly orientation dependent. While oscillations with a long period of ∼120 ns at ($\varphi = 60°$, $\chi = 0°$) reflect the temporal beat pattern of the quadrupole splitting of the LS state, the oscillations with the much shorter period of ∼30 ns at ($\varphi = 80°$, $\chi = -27°$) carry the signature of the HS state as in Fig. 4(a). This observation suggests that at $T = 120$ K there are still iron sites in the HS state, which have not undergone a spin transition to the LS state. In fact, at this particular angular position, the χ-PR-NFS scan in Fig. 3(d) exhibits a deep minimum (black arrow), while the corresponding scan in Fig. 3(a) has a maximum at this position (black arrow). This means that at $\varphi = 80°$, $\chi = -27°$ the signal from the LS majority contribution is strongly suppressed by the polarimeter, thereby enabling the selective detection of the HS minority species that are still present at $T = 120$ K. The beat patterns at the other orientations appear to be a superposition of long-period and short-period oscillation belonging to the LS and HS states. Since a signature from the HS state is clearly visible in the time spectra, it can only come from an ordered HS minority species with an EFG orientation that is different from that of the LS majority species. From fitting the relative contribution of the HS signal in the time spectrum at $\varphi = 80°$, $\chi = -27°$ [(Fig. 4(b), top right panel; the corresponding minimum in the χ-PR-NFS scan is marked by the black arrow in Fig. 3(d)], we obtain a fraction of $a = 0.03(1)$ of the HS state still present at 120 K. Without the crossed polarizers, the signal from the majority LS state would be about a factor of a^{-1} larger, rendering detection of the signal from the HS minority species very difficult if not impossible. Unfortunately, an accurate determination of the EFG orientation of the LS state from the experimental data is hampered by the large number of free parameters at 120 K; i.e., many parameter sets could explain the measured datasets equally well, so that the LS EFG orientation cannot be unambiguously determined from the data. This prevents a fitting of most of the data at 120 K in Figs. 3(d) and 4(b), which is illustrated in more detail in Appendix F.

In future work, many of the limitations encountered at 120 K can be mitigated by optimizing both sample choice and experimental strategy. Using significantly thinner or smaller single crystals, and aligning the beam along the shortest crystal dimension, will reduce the effective thickness and thus suppress dynamical beats, yielding NFS spectra dominated by quantum beats resulting from hyperfine interactions only. This simplification is essential because dynamical beats introduce an additional modulation of the time spectra that is governed by the effective thickness rather than by the hyperfine splitting, making it difficult to disentangle contributions from two superimposed spin species with different quadrupole splittings. Single-crystal NFS time spectra and NFS-polarimetry χ scans provide primarily orientational information. The remaining parameter space (δ, ΔE_Q) can be further constrained by combining fast χ scans (to preselect informative orientations) with a limited set of time-resolved spectra. Such datasets can be recorded nowadays at hard-X-ray free-electron lasers even with the radiation from a single pulse [42]. Accurate DFT-predicted EFG tensors could serve as tight constraints on the Euler angles rather than fully free fit parameters. Finally, improved cryogenic mounting and the use of smaller crystals will promote homogeneous cooling and a well-defined effective thickness for all orientations. Together, these measures should enable a unique and internally consistent determination of the HS and LS hyperfine parameters and EFG orientations, and provide a more reliable basis for studying HS defect states and their local environment in spin-crossover systems.

IV. CONCLUSION

In conclusion, we have employed polarization-resolved nuclear forward scattering of synchrotron radiation as a quantitative probe of charge anisotropies via electric hyperfine interactions in an iron(II) spin-crossover compound. A high-purity crossed-polarizer setup based on Si(840) channel-cut crystals enables efficient detection of nuclear resonant $\sigma \rightarrow \pi$ scattering at 14.4 keV and strongly suppresses the nonresonant background. This allows us to map the orientation of the electric field gradient tensor of the high-spin state in a single crystal of $Fe(PM\text{-}BiA)_2(NCS)_2$ and to follow its reorientation upon cooling into the low-spin state. By combining orientation-dependent PR-NFS with dynamical NFS calculations and density-functional theory, we determine the EFG tensor of the high-spin state and show that it is well reproduced by electronic-structure calculations. At low temperature, where the monoclinic phase is predominantly in the low-spin state, the polarization-selective geometry can be tuned to suppress the signal from the low-spin state that strongly enhances the relative contribution of the residual high-spin species. From the relative PR-NFS intensities, we infer a high-spin minority fraction of a few percent, whose

temporal beat patterns indicate the formation of ordered high-spin domains rather than isolated, strongly perturbed point defects. These results establish PR-NFS as a sensitive, element- and site-selective tool to study electronic anisotropies and their evolution through spin-crossover transitions. Provided suitable x-ray polarizer-analyzer optics are available at the relevant Mössbauer transition energy, the approach is directly transferable to other Mössbauer-active isotopes and to a broad class of metal-containing systems. We note that polarization analysis can, in principle, also be applied in conventional energy-domain Mössbauer spectroscopy using radioactive sources [9]. However, the high-purity polarimetry exploited here relies on the pulsed time structure of synchrotron radiation, which separates the delayed nuclear resonant signal from the prompt electronic scattering. This intrinsic time gating, combined with the nearly nine orders of magnitude suppression of the nonresonant background by the crossed polarizers, provides a signal-to-noise ratio that is very difficult to achieve in the energy domain, where the continuous-wave nature of the radioactive source does not permit temporal discrimination. Nonetheless, for systems with large quadrupole splittings and favorable single-crystal orientations, polarization-dependent conventional Mössbauer spectroscopy [9] remains a valuable complementary approach. In combination with complementary techniques such as conventional Mössbauer spectroscopy, PR-NFS can be used to relate changes in hyperfine parameters to microscopic charge distributions and their anisotropies. The demonstrated capability to detect and characterize small ordered minority phases suggests that PR-NFS is well suited for future studies of ordering phenomena at the onset of phase transitions and, when implemented in a pump-probe geometry, for time-resolved investigations of transient and nonequilibrium electronic states.

ACKNOWLEDGMENTS

We acknowledge the support of the Helmholtz Association through project-oriented funds. Moreover, this work was supported by the German Federal Ministry of Research, Technology and Space (BMFTR) in the frame of the Projects No. 05K16UKA and No. 05K13SJ1, and by the Deutsche Forschungsgemeinschaft (DFG, German Research Foundation) – TRR 173 – 268565370 Spin + X. Within this funding, J.A.W. and V.S. are grateful to Allianz für Hochleistungsrechnen Rheinland-Pfalz (AHRP) for providing CPU time within the project RPTU-SPINPLUSXA4

DATA AVAILABILITY

The data that support the findings of this article are not publicly available. The data are available from the authors upon reasonable request.

APPENDIX A: THE COMPOUND $[Fe(PM\text{-}BiA)_2(NCS)_2]$

A single crystal of $[Fe(PM\text{-}BiA)_2(NCS)_2]$ was prepared using 97% ^{57}Fe enriched $FeSO_4 \cdot 7H_2O$. The obtained sample was synthesized as described in Ref. [33] for phase I. It was then recrystallized by slow evaporation of diethyl ether into the light protected 5:1 CH_2Cl_2/ethanol solution of the complex. X-ray diffraction measurements revealed the monoclinic symmetry of

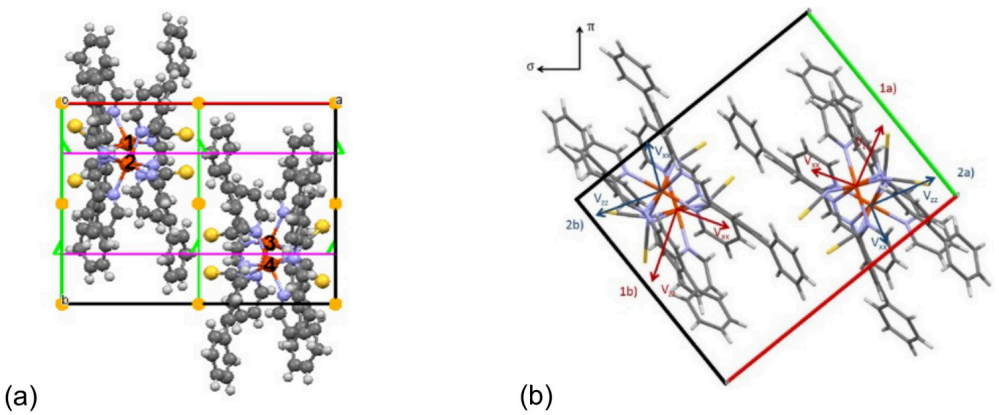


FIG. 5. (a) Schematic representation of the monoclinic phase of $[Fe(PM\text{-}BiA)_2(NCS)_2]$ at room temperature, with viewing direction along the c axis. There are three symmetry operations: inversion centre (yellow), twofold screw axis (green), and a glide plane (purple). (b) Initial orientation ($\varphi = 0°$, $\chi = 0°$) of the single crystal, chosen due to the results of the DFT calculation (see Fig. 3). For the analysis of the experimental data, two different EFG orientations have to be considered for this complex.

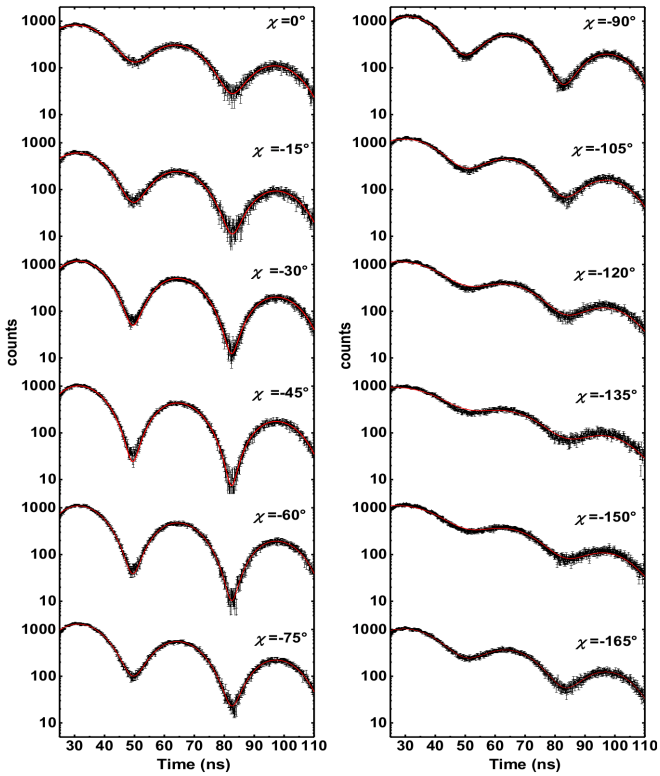


FIG. 6. NFS spectra taken at room temperature without polarization analyzer with a fixed orientation $\varphi = 0^\circ$ and selected orientations χ (for the definition of rotation angle χ, see Fig. 1). The solid lines show theoretical calculations assuming a pure HS state with $\Delta E_Q = 2.58\,(\pm 0.02)$ mm/s and $\eta = 0.3\,(\pm 0.20)$ (see Table I for simulation parameters).

the lattice that is independent of the temperature dependent spin state with small changes of bond lengths and angles related to the HS (298 K) and the LS phase (140 K) [33,43].

APPENDIX B: NFS SPECTRA WITHOUT POLARIZATION ANALYZER TAKEN AT ROOM TEMPERATURE

Figure 6 displays NFS time spectra taken at room temperature without polarization analyzer. Solid red lines are simulations using the software package CONUSS [38,39]. Next to the electric hyperfine parameters, the data analysis includes the dimensionless effective thickness $t_{\rm eff} = d\,\rho_N\,\sigma_N\,f_{\rm LM}\,a$, where d is the geometrical thickness of the sample along the beam direction, ρ_N is the number density of the resonant nuclei, σ_N is the nuclear resonant absorption cross section of ^{57}Fe, $f_{\rm LM}$ is the Lamb-Mössbauer factor, and a is the Mössbauer isotope abundance in the sample. The effective thickness increases with decreasing temperature due to the temperature dependence of $f_{\rm LM}$.

APPENDIX C: NFS SPECTRA WITHOUT POLARIZATION ANALYZER TAKEN AT $T = 120$ K

The interpretation of the spectra for the characterization of the LS state delivers no explicit results in terms of the orientation of the EFG. There are several possibilities to acquire a good agreement between the experimental data and the simulation using CONUSS [38,39]. This is illustrated in Fig. 7 with the parameters used for the simulation of the data listed in Table II . The presented simulations only show one possibility to simulate the experimental data taken at $T = 120$ K.

It must be noted that the resulting beating structure originates not only from the LS EFG, leading to equidistant quantum beats, but there are also dynamical beats superposed. This effect comes into play due to the increased effective thickness $t_{\rm eff}$ at lower temperatures. In addition to the minority HS species, this increased effective thickness also complicates the analysis of the 120-K data.

APPENDIX D: THEORETICAL ANALYSIS OF THE χ-PR-NFS SCANS

For the analysis of the χ-PR-NFS scans, the intensity of the σ-π scattering process in dependence on the orientation of the main axis v_{zz} is evaluated using the dynamical theory of nuclear forward scattering [25,44,45]. The intensity $y(\chi)$ with fixed φ can be described using the off-diagonal element of the (2×2) forward scattering matrix $\mathbf{f}_r$ that describes the polarization dependence of the scattering process. With the consideration of an offset χ_0 depending on the initial orientation of the sample,

TABLE I. Parameters used for the theoretical simulation of the experimental NFS spectra taken at room temperature as shown in Fig. 6. For the theoretical simulation, an EFG asymmetry parameter of $\eta = 0.3$ was used. The maximal errors for t_{eff} and ΔE_Q are ± 1 and ± 0.01 mm/s, respectively. Considering the crystal structure of the investigated crystal, we used two EFG components named 1a and 1b (see Fig. 5) with euler angles α_{1a} and α_{1b} and $\beta = -90^\circ$, $\gamma = -90^\circ$.

φ (deg)	χ (deg)	t_{eff}	ΔE_Q (mm s^{-1})	α_{1a} (deg)	α_{1b} (deg)
0	0	16	2.60	62	32
0	−15	16	2.59	47	17
0	−30	17	2.59	32	2
0	−45	17	2.59	17	−13
0	−60	16	2.59	2	−28
0	−75	16	2.59	−13	−43
0	−90	15	2.59	−28	−58
0	−105	14	2.58	−43	−73
0	−120	14	2.57	−58	−88
0	−135	14	2.56	−73	−103
0	−150	14	2.57	−88	−118
0	−165	15	2.58	−103	−133

this leads to

$$y = y_0 + A[\sin(\chi - \chi_0)\cos(\chi - \chi_0)]^2. \tag{D1}$$

The cartesian coordinates of v'_{zz} resulting from a rotation of the sample performed with the Eulerian cradle can be described theoretically with the help of rotation matrices $\mathbf{R}_y(\varphi)$ and $\mathbf{R}_z(\chi)$ using $v'_{zz} = (x, y, z)$ as start parameters:

$$v'_{zz} = \mathbf{R}_z(\chi)\mathbf{R}_y(\varphi)\, v_{zz}. \tag{D2}$$

The dynamical theory of NFS delivers the result that, for an axially symmetric system, no σ-π scattering occurs if the scalar product of v'_{zz} with $\boldsymbol{\sigma}$ or $\boldsymbol{\pi}$ disappears. Consequently, we can use the following formula to describe the shift in the minima in

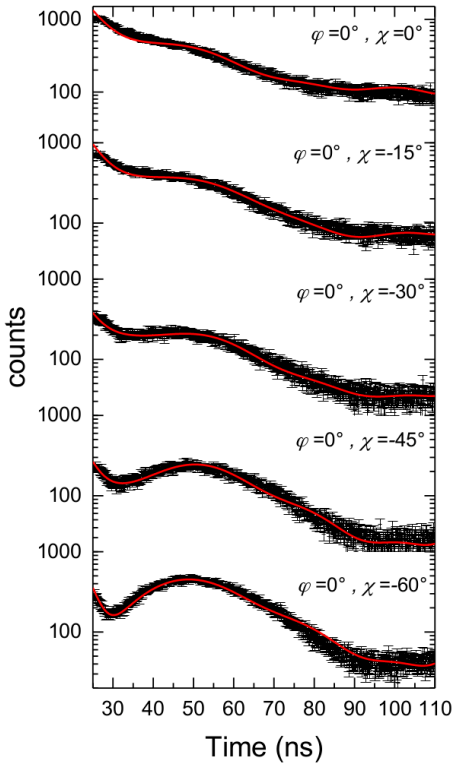


FIG. 7. NFS spectra taken at $T = 120$ K without polarization analyzer with fixed orientation $\varphi = 0^\circ$ and selected orientations χ. The red solid lines show theoretical calculations assuming 93 (± 5)% LS with $\Delta E_Q = 0.63$ (± 0.02) mm/s and 7 (± 5)% HS with $\Delta E_Q = 2.98$ (± 0.20) mm/s. The difference in the isomer shift is $\Delta\delta = \delta_{\text{HS}} - \delta_{\text{LS}} = 0.61$ (± 0.03) mm/s (simulation parameters given in Table II).

TABLE II. Parameters used for the theoretical simulation of the experimental NFS spectra taken at $T = 120$ K (Fig. 7). For the theoretical simulation, a maximal error of ± 1 for t_{eff} is used. The maximal errors of the hyperfine parameters for the LS component are ± 0.02 mm/s for ΔE_Q and ± 0.2 for η. For the HS component, ΔE_Q has a maximal error of ± 0.1 mm/s and $\eta = 0.25 \pm 0.2$, and the area is accurate within an error of $\pm 5\%$. The determination of the Euler angles ($\alpha, \beta = 0^\circ/180^\circ, \gamma = 0^\circ$) delivers a tolerance of $\pm 5^\circ$ and the maximal error for the difference of the isomer shifts $\delta_{\text{HS}} - \delta_{\text{LS}}$ is ± 0.02 mm/s. Please note that the presented simulation only shows one possibility to simulate the experimental data. In order to determine the exact magnitude and orientation of the EFG, more experimental data than could be acquired are necessary.

			LS				HS		$\delta_{\text{HS}} - \delta_{\text{LS}}$
φ (deg)	χ (deg)	t_{eff}	η	ΔE_Q (mm s^{-1})	α_1 (deg)	α_2 (deg)	Weight (%)	ΔE_Q (mm s^{-1})	(mm s^{-1})
0	0	45	0.45	0.65	−149	−138	9	3.07	0.59
0	−15	49	0.45	0.64	−165	−155	9	2.99	0.61
0	−30	51	0.45	0.64	−185	−161	11	2.94	0.61
0	−45	59	0.26	0.63	−200	−175	10	2.95	0.61
0	−60	63	0.25	0.61	−218	−190	8	2.96	0.62

dependency of the angle χ with fixed φ:

$$\tan \chi = \frac{-y}{x \cos \varphi + z \sin \varphi}. \tag{D3}$$

With this calculation, the experimentally determined orientation dependency of the intensity of the NFS polarimetry scattering process can be analyzed, leading to an approximation of the EFG orientation at the Fe nucleus of the investigated molecule.

APPENDIX E: TABLES WITH SIMULATION PARAMETERS

This Appendix displays the lists of parameters that were used for the analysis of the data shown in Figs. 2–4.

TABLE III. Parameters used for the theoretical simulation of the experimental PR-NFS spectra taken at $T = 220$ K for $\varphi = 0^\circ$ [Fig. 2(a)] and $\varphi \neq 0^\circ$ [Fig. 4(a)], with $\eta = 0.3 \pm 0.2$. The maximal error for t_{eff} is ± 1 and 0.05 mm/s for ΔE_Q due to the low intensity, Euler angles for $\varphi = 0^\circ$ are as given in Table I. The Euler angles for $\varphi = 80^\circ$, $\chi = -27^\circ$ are $\alpha_{1a} = 58^\circ$, $\beta_{1a} = 62^\circ$, $\gamma_{1a} = 11^\circ$, $\alpha_{1b} = 132^\circ$, $\beta_{1b} = 147^\circ$, and $\gamma_{1b} = 18^\circ$. The Euler angles for $\varphi = 90^\circ$, $\chi = -40^\circ$ are $\alpha_{1a} = 50^\circ$, $\beta = 148^\circ$, $\gamma = 0^\circ$, $\alpha_{1b} = -130^\circ$, $\beta = 62^\circ$, and $\gamma = 0^\circ$.

φ (deg)	χ (deg)	t_{eff}	ΔE_Q (mm s^{-1})
0	0	12	2.67
0	−15	11	2.67
0	−30	10	2.67
0	−45	10	2.65
0	−75	11	2.65
0	−90	10	2.64
90	−40	8	2.57
80	−27	8	2.57

TABLE IV. Parameters of the analysis of the χ-PR-NFS scans shown in Figs. 3(a) and 3(b). χ_{Min} denotes the angle where a minimum of the count rate in the χ-PR-NFS scan is observed (with a maximal error of $\pm 2^\circ$). The parameter χ_0 is used to simulate the experimental data [see Fig. 3(a)]. Δt denotes the time interval used for data acquisition for each crystal orientation φ, χ. The simulation in Fig. 3(b) is based on $v_{zz} = (\cos\alpha, \sin\alpha, 0)$ with $\alpha = 47^\circ$ for $\varphi = 0^\circ$, $\chi = 0^\circ$.

φ (deg)	T	Δt (s)	χ_{Min} (deg)	χ_0 (deg)
0	220 K	10	−47.5	47
45	RT	10	−54.0	55
65	RT	10	−68.8	69
80	RT	10	−78.5	79
90	220 K	15	−87.0	87

APPENDIX F: ANALYSIS OF LOW-TEMPERATURE DATA

In analogy to the approach used for the data analysis for the HS state ($T \geqslant 220$ K), an attempt was made to analyze the NFS and PR-NFS data taken at $T = 120$ K using the DFT results as initial parameter set for the LS EFG. However, the use of

TABLE V. Parameters of the analysis of the χ-PR-NFS scans taken at $T = 120$ K, shown in Figs. 3(d) and 3(e). χ_{Min} denotes the angle where a minimum of the count rate in the χ-PR-scan is observed, with the maximum error of the estimation given by $\Delta\chi_{\mathrm{min}}$. The data acquisition time for each crystal orientation φ, χ was $\Delta t = 20$ s. The simulation in Fig. 3(d) is based on $v_{zz} = (\cos\alpha, \sin\alpha, 0)$ with $\alpha = 34^\circ$ for $\varphi = 0^\circ$, $\chi = 0^\circ$.

φ (deg)	110	100	95	90	85	80	70	60	45	30	0
χ_{Min} (deg)	−60	−66	−77	−90	−108	−115	−128	−134	−135	−140	−135
$\Delta\chi_{\mathrm{Min}}$ (deg)	5	5	5	5	5	5	5	8	8	8	8

this orientation did not lead to any result allowing to reproduce all the available datasets consistently. Thus, the large number of unknown parameters in that case, i.e., the LS electric field gradient with two LS sites with three angles each and the unknown asymmetry parameter η hampers the determination of an adequate simulation. Moreover, the fact that the percentage of the residual HS EFG with its EFG orientation is not explicitly known complicates the analysis. The fact that the two latter aspects have a decisive influence on the data is reflected in the simulated χ-PR-NFS scans, as shown in Figs. 8 and 9. These simulations indicate and explain why there are many parameter sets that could explain the measured data equally well, so that the LS EFG orientation cannot be unambiguously determined from the data.

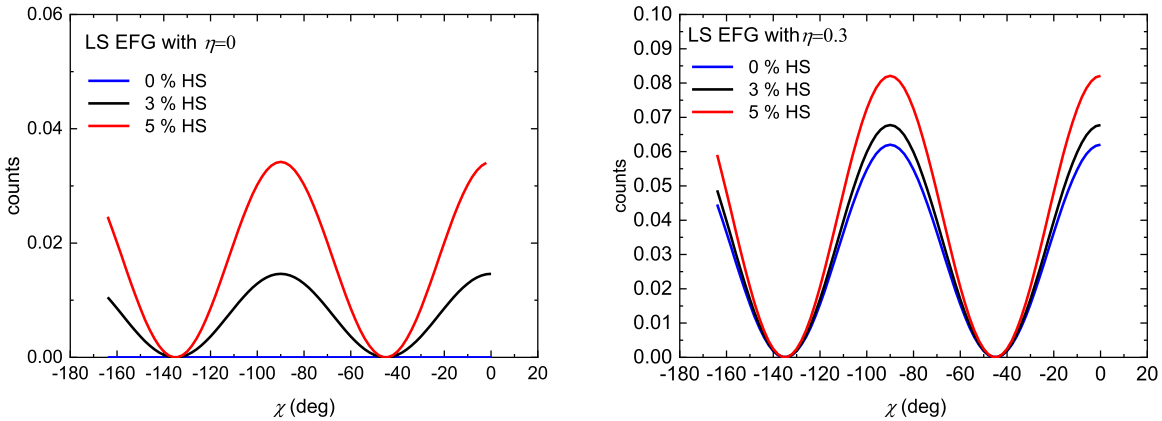


FIG. 8. Simulated χ-PR-NFS scans using a fictive LS EFG orientation with $V_{zz} \parallel k_0$ and the HS EFG in such a way that $V_{yy} \parallel k_0$ and V_{zz} in the σ-π plane with $\alpha = \measuredangle(V_{yy}, \sigma) = 45^\circ$ at $\varphi = 0^\circ$, $\chi = 0^\circ$, with different asymmetry parameters for the LS EFG (as indicated). This asymmetry parameter significantly influences the contrast (difference between maximum and minimum signal) in the χ scans.

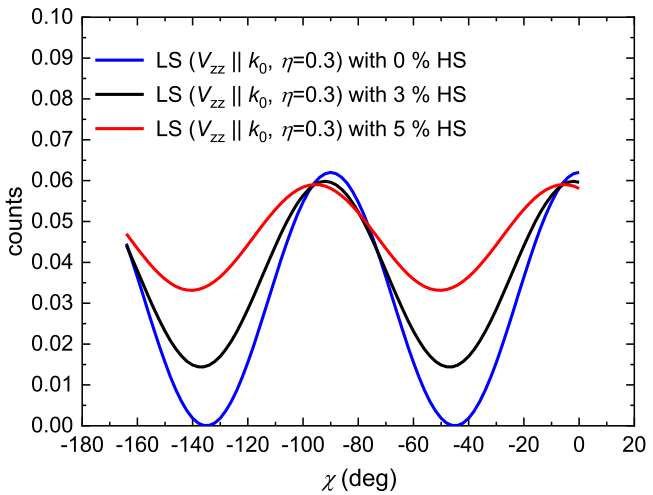


FIG. 9. Simulated χ-PR-NFS scans using a fictive LS EFG orientation with $V_{zz} \parallel k_0$ and the HS EFG in such a way that $V_{yy} \parallel k_0$ and V_{zz} in the σ-π plane with $\alpha = \measuredangle(V_{yy}, \sigma) = 0^\circ$ at $\varphi = 0^\circ$, $\chi = 0^\circ$. Here, the percentage of the HS strongly influences the contrast the maxima/minima position of the χ-PR-NFS scans.

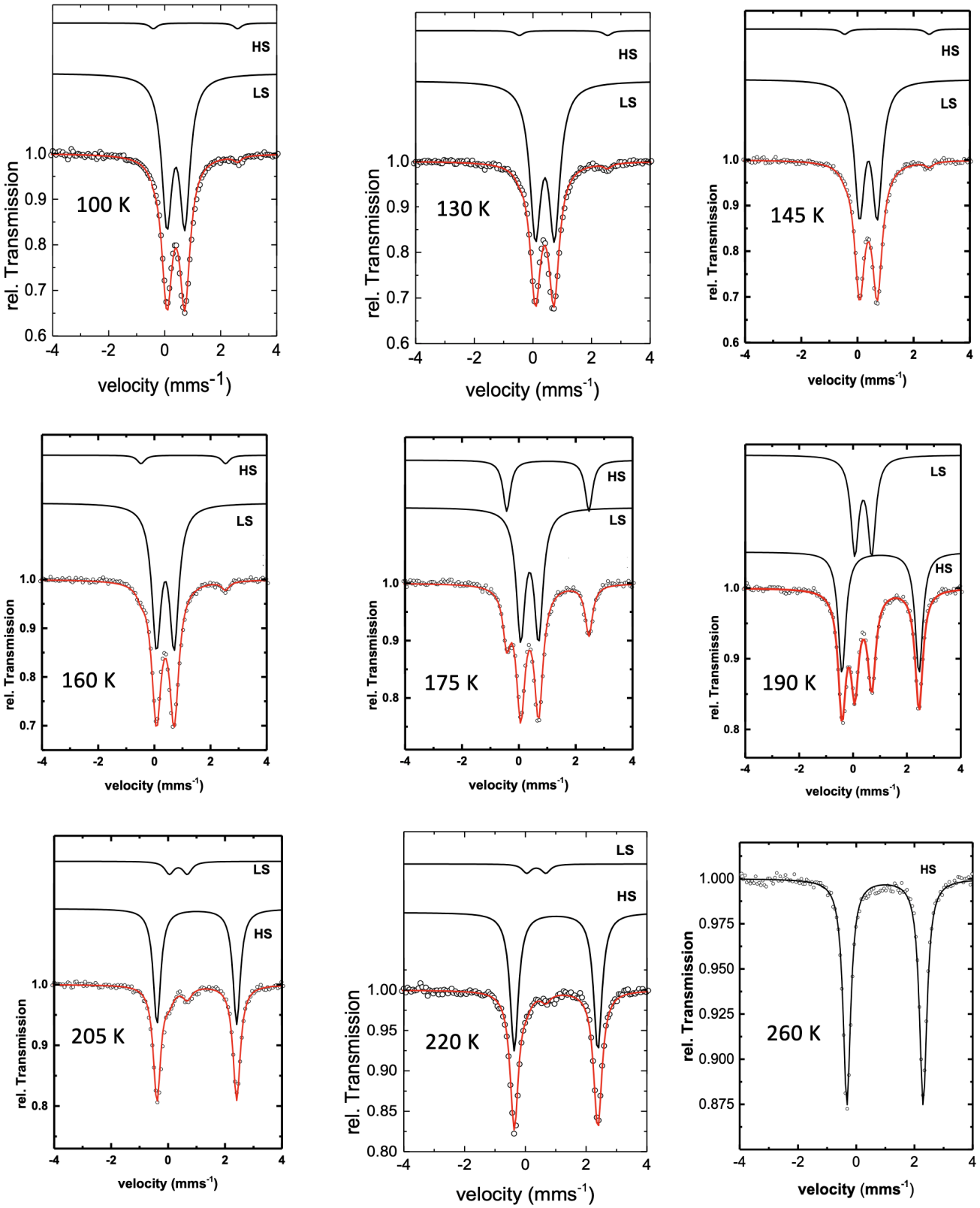


FIG. 10. Mössbauer transmission spectra recorded to determine the SCO properties on polycrystalline [Fe(PM-BiA)$_2$(NCS)$_2$] for temperatures indicated, analyzed by the thin absorber approximation using the Excel macro Vinda [46]. For fitting, two doublets are used for $T < 260$ K, and one doublet for $T \geqslant 260$ K, each with Lorentzian line profile (see Table VI for parameters).

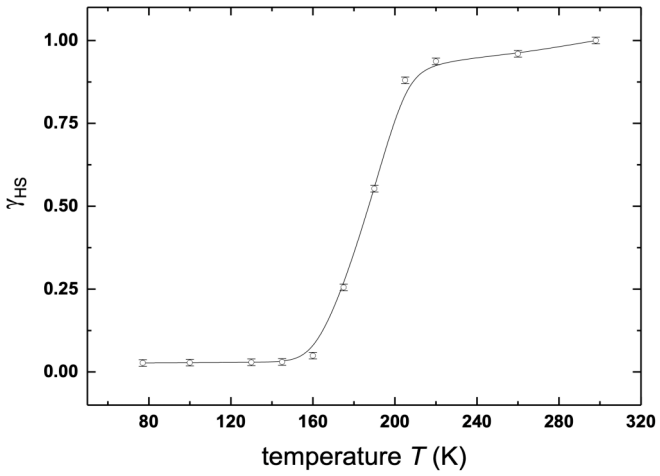


FIG. 11. Molar high-spin fraction γ_{HS} (HS fraction normalized to area of the total Mössbauer spectrum) of polycrystalline [Fe(PM-BiA)$_2$(NCS)$_2$] as a function of temperature, calculated using the relative HS contributions listed in Table VI, determined from the transmission spectra in Fig. 10. The solid line is a guide to the eye.

APPENDIX G: MÖSSBAUER DATA OF [Fe(PM-BiA)$_2$(NCS)$_2$] POWDER SAMPLES

To illustrate the SCO of the polycrystalline precursor material for single-crystal growth, Mössbauer transmission spectra were taken as a function of temperature, as shown in Fig. 10. Hyperfine parameters δ and ΔE_Q are displayed together with the area fractions of the HS state in Table VI. The spin transition is illustrated by plotting the area fraction of the HS state as a function of temperature in Fig. 11. The spin transition is a gradual SCO as typical for the monoclinic phase [33] with a transition temperature of $T_{1/2} = 187$ K. This is close to the transition temperature of the monoclinic modification for which magnetic susceptibility measurements indicate that $T_{1/2} = 190$ K, while $T_{1/2}\downarrow = 168$ K and $T_{1/2}\uparrow = 173$ K were found for the orthorhombic polymorph [33]. It can thus be concluded that the powder sample used here dominantly contains the monoclinic polymorph of [Fe(PM-BiA)$_2$(NCS)$_2$].

TABLE VI. Mössbauer parameters of polycrystalline [Fe(PM-BiA)$_2$(NCS)$_2$] determined using Excel macro Vinda [46] for the temperature range from $T = 77$ K to RT (selected spectra, see Fig. 10). Experimental errors are ± 0.03 mm/s for ΔE_Q. For T $>$ 175 K, the inaccuracy of δ_{HS} is ± 0.02 mm/s and for δ_{LS} it is ± 0.04 mm/s; for T $<$ 175 K, the inaccuracy of δ_{HS} is ± 0.04 mm/s and for δ_{LS} it is ± 0.02 mm/s. The experimental error of the linewidths is ± 0.03 mm/s, and of the relative contribution it is $\pm 0.5\%$.

	HS				LS				
T	Rel. contribution	δ	ΔE_Q	Γ	Rel. contribution	δ	ΔE_Q	Γ	δ_{HS}- δ_{LS}
(K)	(%)	(mms^{-1})	(mms^{-1})	(mms^{-1})	(%)	(mms^{-1})	(mms^{-1})	(mms^{-1})	(mms^{-1})
298	100	0.97	2.50	0.28	----	----	----	----	----
260	100	0.99	2.62	0.31	----	----	----	----	----
220	93.7	1.01	2.75	0.33	6.3	0.36	0.63	0.35	0.65
205	88.5	1.01	2.80	0.33	11.5	0.36	0.63	0.34	0.65
190	55.3	1.02	2.86	0.33	44.7	0.38	0.63	0.38	0.64
175	25.5	1.02	2.89	0.33	74.5	0.38	0.63	0.37	0.64
160	4.9	1.03	3.01	0.33	95.1	0.39	0.63	0.40	0.64
145	3.0	1.03	3.01	0.33	97.0	0.39	0.63	0.43	0.64
130	2.9	1.04	3.01	0.33	97.1	0.39	0.63	0.43	0.65
100	2.8	1.10	3.01	0.33	97.2	0.40	0.64	0.45	0.70
77	2.7	1.12	3.05	0.33	97.3	0.41	0.65	0.46	0.71

[1] C. Kramer, A. Spinn, and K. R. Liedl, Charge anisotropy: Where atomic multipoles matter most, J. Chem. Theory Comput. **10**, 4488 (2014).

[2] B. Nordén, A. Rodger, and T. Dafforn, *Linear Dichroism and Circular Dichroism* (The Royal Society of Chemistry, Cambridge, 2010).

[3] D. Che, D. B. Shapiro, R. M. Esquerra, and D. S. Kliger, Ultrasensitive time-resolved linear dichroism spectral measurements using near-crossed linear polarizers, Chem. Phys. Lett. **224**, 145 (1994).

[4] J. Réhault, V. Zanirato, M. Olivucci, and J. Helbing, Linear dichroism amplification: Adapting a long-known technique for ultrasensitive femtosecond IR spectroscopy, J. Chem. Phys. **134**, 124516 (2011).

[5] G. van der Laan, B. T. Thole, G. A. Sawatzky, J. B. Goedkoop, J. C. Fuggle, J.-M. Esteva, R. Karnatak, J. P. Remeika, and H. A. Dabkowska, Experimental proof of magnetic X-ray dichroism, Phys. Rev. B **34**, 6529 (1986).

[6] G. Schütz, W. Wagner, W. Wilhelm, P. Kienle, R. Zeller, R. Frahm, and G. Materlik, Absorption of circularly polarized X-rays in iron, Phys. Rev. Lett. **58**, 737 (1987).

[7] S. Lovesey and S. Collins, *X-ray Scattering and Absorption by Magnetic Materials*, Oxford Series on Synchrotron Radiation (Clarendon Press, Oxford, 1996).

[8] J. Stöhr and H. C. Siegmann, *Magnetism* (Springer, Berlin, 2006).

[9] K. Szymański, Polarized radiation in Mössbauer spectroscopy, Phys. Rep. **423**, 295 (2006).

[10] T. Mitsui, Y. Imai, R. Masuda, M. Seto, and K. Mibu, ^{57}Fe polarization-dependent synchrotron Mössbauer-spectroscopy using a diamond phase plate and an iron borate nuclear Bragg-monochromator, J. Synchrotron Radiat. **22**, 427 (2015).

[11] M. A. Andreeva, R. A. Baulin, O. V. Slinko, L. Häggström, V. E. Asadchikov, D. N. Karimov, B. S. Roshchin, D. A. Ponomarev, L. N. Romashev, A. I. Chumakov, D. Bessas, and R. Rüffer, Polarization selection in Mössbauer reflectivity for magnetic multilayer investigation, J. Phys.: Conf. Ser. **1389**, 012016 (2019).

[12] B. Marx, K. S. Schulze, I. Uschmann, T. Kämpfer, R. Lötzsch, O. Wehrhan, W. Wagner, C. Detlefs, T. Roth, J. Härtwig, E. Förster, T. Stöhlker, and G. G. Paulus, High-precision X-ray polarimetry, Phys. Rev. Lett. **110**, 254801 (2013).

[13] B. Marx-Glowna, I. Uschmann, K. S. Schulze, H. Marschner, H.-C. Wille, K. Schlage, T. Stöhlker, R. Röhlsberger, and G. G. Paulus, Advanced X-ray polarimeter design for nuclear resonant scattering, J. Synchrotron Radiat. **28**, 120 (2021).

[14] K. S. Schulze, Fundamental limitations of the polarization purity of X-rays, APL Photon. **3**, 126106 (2018).

[15] D. P. Siddons, M. Hart, Y. Amemiya, and J. B. Hastings, X-ray optical activity and the Faraday effect in cobalt and its compounds, Phys. Rev. Lett. **64**, 1967 (1990).

[16] M. Hart, D. P. Siddons, Y. Amemiya, and V. Stojanoff, Tunable X-ray polarimeters for synchrotron radiation sources, Rev. Sci. Instrum. **62**, 2540 (1991).

[17] A. T. Schmitt, Y. Joly, K. S. Schulze, B. Marx-Glowna, I. Uschmann, B. Grabiger, H. Bernhardt, R. Loetzsch, A. Juhin, J. Debray, H.-C. Wille, H. Yavas, G. G. Paulus, and R. Röhlsberger, Disentangling X-ray dichroism and birefringence via high-purity polarimetry, Optica **8**, 56 (2021).

[18] T. S. Toellner, E. E. Alp, W. Sturhahn, T. M. Mooney, X. Zhang, M. Ando, Y. Yoda, and S. Kikuta, Polarizer/analyzer filter for nuclear resonant scattering of synchrotron radiation, Appl. Phys. Lett. **67**, 1993 (1995).

[19] D. Siddons, J. Hastings, U. Bergmann, F. Sette, and M. Krisch, Mössbauer spectroscopy using synchrotron radiation: Overcoming detector limitations, Nucl. Instrum. Methods Phys. Res. Sect. B **103**, 371 (1995).

[20] R. Röhlsberger, E. Gerdau, R. Rüffer, W. Sturhahn, T. Toellner, A. Chumakov, and E. Alp, X-ray optics for μeV-resolved spectroscopy, Nucl. Instrum. Methods Phys. Res. Sect. A **394**, 251 (1997).

[21] E. Alp, W. Sturhahn, and T. Toellner, Polarizer–analyzer optics, Hyperfine Interact. **125**, 45 (2000).

[22] K. P. Heeg, H.-C. Wille, K. Schlage, T. Guryeva, D. Schumacher, I. Uschmann, K. S. Schulze, B. Marx, T. Kämpfer, G. G. Paulus, R. Röhlsberger, and J. Evers, Vacuum-assisted generation and control of atomic coherences at X-Ray energies, Phys. Rev. Lett. **111**, 073601 (2013).

[23] J. Haber, K. S. Schulze, K. Schlage, R. Loetzsch, L. Bocklage, T. Gurieva, H. Bernhardt, H.-C. Wille, R. Rüffer, I. Uschmann, G. G. Paulus, and R. Röhlsberger, Collective strong coupling of X-rays and nuclei in a nuclear optical lattice, Nat. Photon. **10**, 445 (2016).

[24] B. Marx-Glowna, B. Grabiger, R. Lötzsch, I. Uschmann, A. T. Schmitt, K. S. Schulze, A. Last, T. Roth, S. Antipov, H.-P. Schlenvoigt, I. Sergueev, O. Leupold, R. Röhlsberger, and G. G. Paulus, Scanning high-sensitive X-ray polarization microscopy, New J. Phys. **24**, 053051 (2022).

[25] R. Röhlsberger, *Nuclear Condensed Matter Physics with Synchrotron Radiation*, Springer Tracts in Modern Physics (Springer-Verlag, Berlin, 2004), Vol. 208.

[26] P. Gütlich, A. Hauser, and H. Spiering, Thermal and optical switching of iron(II) complexes, Angew. Chem. Int. Ed. Engl. **33**, 2024 (1994).

[27] O. Kahn and C. J. Martinez, Spin-transition polymers: From molecular materials toward memory devices, Science **279**, 44 (1998).

[28] P. Gütlich and H. A. Goodwin, Spin crossover—An overall perspective, in *Spin Crossover in Transition Metal Compounds I*, edited by P. Gütlich and H. Goodwin (Springer, Berlin, 2004), pp. 1–47.

[29] M. Halcrow, *Spin-Crossover Materials: Properties and Applications* (Wiley, Chichester, 2013).

[30] T. G. Gopakumar, F. Matino, H. Naggert, A. Bannwarth, F. Tuczek, and R. Berndt, Electron-induced spin crossover of single molecules in a bilayer on gold, Angew. Chem. Int. Ed. **51**, 6262 (2012).

[31] E. Ruiz, Charge transport properties of spin crossover systems, Phys. Chem. Chem. Phys. **16**, 14 (2014).

[32] N. Baadji and S. Sanvito, Giant resistance change across the phase transition in spin-crossover molecules, Phys. Rev. Lett. **108**, 217201 (2012).

[33] J.-F. Létard, G. Chastanet, O. Nguyen, S. Marcén, M. Marchivie, P. Guionneau, D. Chasseau, and P. Gütlich, Spin crossover properties of the [Fe(*PM-BiA*)$_2$(NCS)$_2$] complex—*Phases I* and *II*, Monatsh. Chem. **134**, 165 (2003).

[34] W. Nicolazzi and A. Bousseksou, Thermodynamical aspects of the spin crossover phenomenon, C. R. Chim. **21**, 1060 (2018).

[35] http://photon-science.desy.de/facilities/petra_iii/beamlines/p01_dynamics/index_eng.html.

[36] S. Rackwitz, I. Faus, M. Schmitz, H. Kelm, H.-J. Krüger, K. K. Andersson, H.-P. Hersleth, K. Achterhold, K. Schlage, H.-C. Wille, V. Schünemann, and J. A. Wolny, A new sample environment for cryogenic nuclear resonance scattering experiments on single crystals and microsamples at P01, PETRA III, Hyperfine Interact. **226**, 673 (2014).

[37] M. J. Frisch, G. W. Trucks, H. B. Schlegel, G. E. Scuseria, M. A. Robb, J. R. Cheeseman, G. Scalmani, V. Barone, B. Mennucci, G. A. Petersson, *et al.*, Gaussian 09 Revision E.01, Gaussian Inc., Wallingford, CT, 2009.

[38] W. Sturhahn, CONUSS and PHOENIX: Evaluation of nuclear resonant scattering data, Hyperfine Interact. **125**, 149 (2000).

[39] CONUSS is free software. It can be obtained via the software site http://www.nrixs.com.

[40] DFT calculations were performed using Gaussian09 [37] with the functional B3LYP and the basis CEP-31G. We used a model molecule (shown in Fig. 3) with one of the rings of biphenyl replaced with hydrogen in order to approximate the molecule with C_2 symmetry (compare with Fig. 5).

[41] L. Scherthan, Polarimetrie mit resonanter Kernstreuung, Diploma Thesis, Technische Universität Kaiserslautern, Fachbereich Physik, 2016.

[42] M. Gerharz, W. Hippler, B. Marx-Glowna, S. Sadashivaiah, K. S. Schulze, I. Uschmann, R. Lötzsch, K. Schlage, S. Velten, D. Lentrodt, *et al.*, Single-shot sorting of Mössbauer time-domain data at X-ray free electron lasers, arXiv:2509.15833.

[43] J.-F. Létard, P. Guionneau, L. Rabardel, J. A. K. Howard, A. E. Goeta, D. Chasseau, and O. Kahn, Structural, magnetic, and photomagnetic studies of a mononuclear iron(ii) derivative exhibiting an exceptionally abrupt spin transition. Light-induced thermal hysteresis phenomenon, Inorg. Chem. **37**, 4432 (1998).

[44] J. Hannon and G. Trammell, Coherent γ-ray optics, Hyperfine Interact. **123**, 127 (1999).

[45] D. Siddons, U. Bergmann, and J. Hastings, Polarization effects in resonant nuclear scattering, Hyperfine Interact. **123**, 681 (1999).

[46] H. P. Gunnlaugsson, Spreadsheet based analysis of Mössbauer spectra, Hyperfine Interact. **237**, 79 (2016).